

# Molecular Design of Amorphous Porous Organic Cages for Enhanced Gas Storage

Jack D. Evans,<sup>§</sup> David M. Huang,<sup>§</sup> Matthew R. Hill,<sup>†</sup> Christopher J. Sumbly,<sup>§</sup> David S. Sholl,<sup>‡</sup> Aaron W. Thornton,<sup>\*,†</sup> and Christian J. Doonan<sup>\*,§</sup>

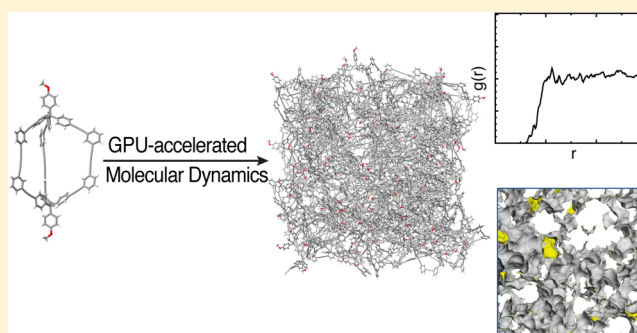
<sup>†</sup>CSIRO Manufacturing Flagship, Clayton, Victoria 3169, Australia

<sup>‡</sup>School of Chemical and Biomolecular Engineering, Georgia Institute of Technology, Atlanta, Georgia 30332, United States

<sup>§</sup>Centre for Advanced Nanomaterials, School of Physical Sciences, University of Adelaide, Adelaide, South Australia 5005, Australia

## Supporting Information

**ABSTRACT:** Porous molecular solids are garnering increasing attention with examples of high surface areas and applications in molecular separations. Recently, amorphous networks of molecular cages have shown increased porosity with respect to their crystalline counterparts. However, the structures of amorphous materials cannot be precisely elucidated by X-ray diffraction techniques, thus molecular simulations are vital to understanding their pore structures and the origin of porosity. Here, we use GPU-accelerated molecular dynamics simulations as an efficient methodology to construct representative amorphous network structures. We employ Voronoi network analysis of amorphous networks of seven previously reported cage molecules to provide insight into structure–property relationships. Accordingly, we apply this understanding to delineate synthetic design features that give rise to highly porous analogues of chemically robust cages constructed from carbon–carbon bonds.



## INTRODUCTION

Porous solids are widely researched for their application to heterogeneous catalysis,<sup>1</sup> gas storage,<sup>2</sup> and molecular separations.<sup>3</sup> The majority of such materials are extended networks with interconnected pore channels that facilitate diffusion of adsorbates throughout the material. Recently, solids composed of shape-persistent organic cage molecules have been investigated for their bulk porosity.<sup>4</sup> In contrast to extended materials, such as metal–organic frameworks<sup>5</sup> (MOFs) or zeolites,<sup>6</sup> these discrete cages are soluble and thus may be readily fabricated into composite materials such as mixed-matrix membranes.<sup>7,8</sup>

Porosity in molecular solids can arise from the interconnection of the cage pores (intrinsic porosity), voids surrounding the cages that result from inefficient packing (extrinsic porosity), or a combination of both.<sup>9</sup> Accordingly, intermolecular packing has a dramatic effect on the surface accessibility of the bulk solids. This is clearly demonstrated in recent work by Doonan et al., in which two different polymorphs of the same molecule gave rise to vastly different N<sub>2</sub> uptakes.<sup>10</sup> Structure-dependent porosity has also been reported by Cooper et al. for imine-based cages.<sup>11</sup> Identifying the origin of porosity is most easily achieved via X-ray diffraction experiments; however, in cases where the bulk solid is amorphous, precisely characterizing the pore structure can be challenging. Consequently, the development of nonstructural

methods for understanding gas diffusion in such materials is necessary.

Molecular simulations have been used to provide insight into the porosity of disordered systems, such as polymers and rigid molecules.<sup>12,13</sup> Recently, Jiang et al. demonstrated an atomistic understanding of H<sub>2</sub>/N<sub>2</sub> separations in amorphous porous solids composed of organic cages of tetrahedral geometry.<sup>14</sup> In the present study, we have improved upon this approach by employing a GPU-accelerated molecular dynamics process to simulate substantially larger amorphous cage networks comprising 100 cages, which was found necessary to adequately sample the configuration space of the porous networks. We simulated amorphous networks of nine cage structures, depicted in Figure 1, to provide insight into how the porosity of these systems can be optimized.

The cage molecules used in this investigation were selected as they encompass a range of geometries, internal volumes, and external functionalities, as shown in Supporting Information (SI) Table SI-1. Specifically, CC1 and CC3 have equivalent volumes but possess different exohedral functionality. CC5 is topologically equivalent to CC1 and CC3 but has approximately 3.8 times the internal pore volume. Cage D1 is of

Received: December 29, 2014

Revised: March 1, 2015

Published: March 4, 2015

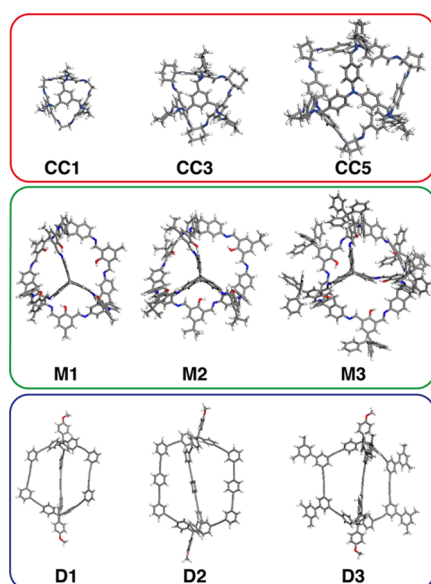


**Figure 1.** Molecular structures of cages investigated. The structures CC1, CC3, CC5, M1–M3, and D1 have been synthesized, but D2 and D3 are hypothetical structures.

trigonal dipyramidal geometry and is constructed from “rod-like” alkyne moieties that give rise to very large window sizes and internal voids. Finally, cages M1–M3 are of octahedral geometry with identical internal volumes, but are differentiated by their external functionality: methyl (M1), *t*-butyl (M2), and triphenylmethyl (M3).<sup>15</sup> Analysis of these systems, which have been synthesized and characterized experimentally, afforded design principles for optimizing the bulk porosity of amorphous solids composed of organic cage molecules. These principles were applied to generate the hypothetical cages D2 and D3 in Figure 1. We determined that for amorphous systems, decorating the surface of cage D1 with sterically demanding groups gives rise to large voids in the packing structure and thus higher surface area.

## ■ SIMULATION METHODOLOGY

Molecular dynamics simulations were employed using the LAMMPS GPU-accelerated code.<sup>16,17</sup> A judicious choice of the force field is critical for ensuring that the packing and structural properties are accurately described. Accordingly, we used a cage-specific force field for the structures that was developed exclusively for imine cage systems.<sup>18</sup> Parameters not listed in the cage-specific force field were taken from a polymer-specific force field<sup>19</sup> that was used as the basis for the cage-specific force field. Long-range electrostatic interactions were calculated using the PPPM method.<sup>20</sup> A Nosé–Hoover thermostat and barostat were used to fix the temperature and pressure of the simulations.<sup>21</sup> Notably, the cages CC1 and CC3 exist in two

different conformers as investigated by Jelfs and co-workers.<sup>22</sup> We have simplified the systems, herein, by simulating only tetrahedral conformers, specifically CC1-R and CC3-R enantiomers.

The simulation procedure used in this study is outlined in Figure 2. In the loading stage, the simulation cells were packed with 100 molecular cage structures at a density of  $0.1 \text{ g}\cdot\text{cm}^{-3}$ , as performed by the amorphous cell module in Materials Studio 6.0. A low-density structure was used to ensure that interlocking of cage molecules or ring sparring was minimized. The assembly step comprised an NVT molecular dynamics simulation at 300 K for 500 ps with a step size of 1 fs. As depicted in Figure 3, this assembly step equilibrates the low-

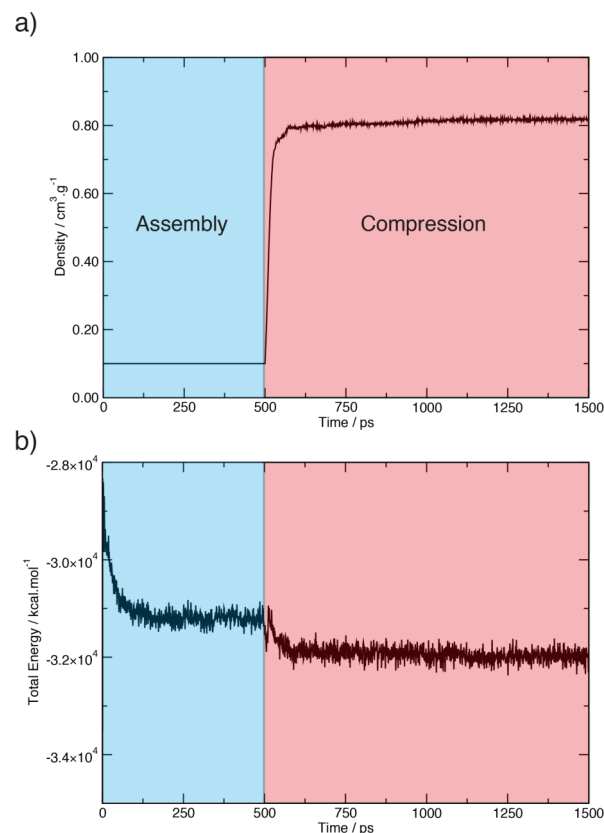


**Figure 3.** Representative sample of the density and total energy during assembly and compression steps of the generation procedure.

density structure, allowing for self-assembly and aggregation of molecules. Following the assembly step was the compression step, which was composed of an NPT molecular dynamics simulation with 1000 atm of external pressure applied at 300 K for 1000 ps with a step size of 1 fs. During this step, the simulation cell shrinks to give a reasonable target density for

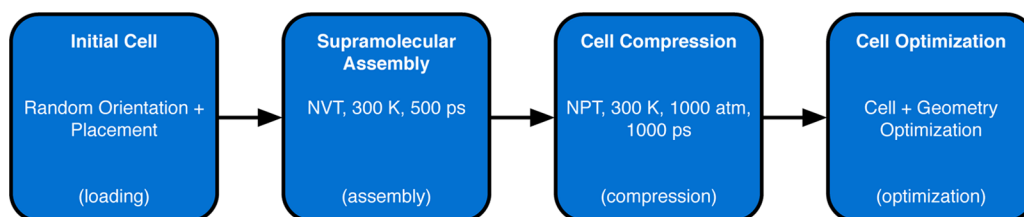


**Figure 2.** Outline of simulation procedure used for production of amorphous cells.

the amorphous structure when compared with an experimentally measured density of a known amorphous cage structure.<sup>23</sup> Finally, the amorphous system and simulation cell were optimized by minimizing the system energy to give a final amorphous structure for subsequent analysis, as shown in Figure 4. The generation procedure was repeated for 10

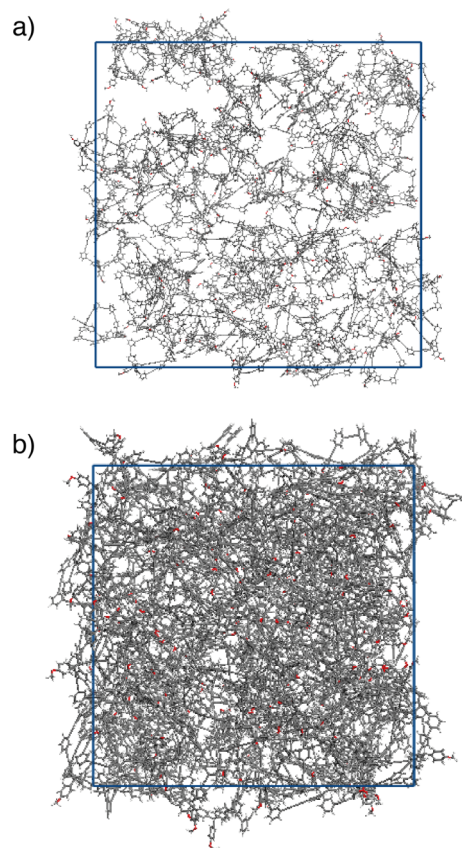


**Figure 4.** Example of structure **D1** at the loading step (density of  $0.10 \text{ g}\cdot\text{cm}^{-3}$ ) and after the minimization step (density of  $0.78 \text{ g}\cdot\text{cm}^{-3}$ ).

independent, randomly generated initial configurations so as to sample the amorphous structural landscape and to allow the sensitivity of the amorphous porous structure to initial conditions to be quantified. All analyses discussed below are averaged over these 10 independent representations of the amorphous structure.

This procedure was adapted from the work of Jiang et al., with the addition of cell compression performed under an external pressure of 1000 atm. The generation methodology of Jiang and co-workers<sup>14</sup> required over  $16 \times 10^6$  steps, whereas in this work we were able to decrease this to  $2 \times 10^6$  molecular dynamic steps. To ensure the compression pressure did not collapse the cage molecules, we tested it on crystalline cells of **CC1**, **CC3**, **CC5**, **D1**, and **M1** and found the external pressure did not appreciably compress the molecules or cells, as shown in SI Table SI-2.

Geometric surface areas and pore volumes for the amorphous systems were calculated using the Zeo++ code. This code uses a Voronoi network to obtain a representation of the pore space for a periodic system.<sup>24,25</sup> For a specified probe size Zeo++ can determine the accessible and inaccessible pore volume. Importantly, soft materials such as porous organic cages have been reported to have dynamic connectivity

between accessible and inaccessible regions. This has been investigated in crystalline materials,<sup>26</sup> but has not been elucidated for amorphous systems owing to the disordered alignment of pores. As a consequence, we have defined the total surface area and pore volume as the sum of the accessible and inaccessible regions as defined by Zeo++ so that regions accessible by dynamic pore-opening events are not overlooked. Finally, extrinsic volumes were calculated for He probe sizes and by blocking the internal cage volume with a sphere of size equivalent to the internal van der Waals diameter of the cage, as shown in SI Table SI-3.

## RESULTS AND DISCUSSION

### Effect of System Size on Porosity and Density of **CC3**.

One of the primary challenges encountered when simulating amorphous materials is to efficiently capture the disorder of a real system with finite periodic simulation cells. To accurately describe such systems, large periodic cells combined with many independent iterations are required. The methodology employed in this study allows us to efficiently simulate cells with more than 100 molecules. We note that a previous report used cells that contained a maximum of 60 molecules.<sup>14</sup> As a test, we chose to study the resulting density and porosity of **CC3** as a function of the number of cage molecules per periodic cell. **CC3** was chosen for this preliminary investigation as it had been previously studied in detail by Cooper et al. Figure 5 shows that the average density and total surface area of the amorphous networks are essentially the same for all system sizes studied, but a significant change in the variance is observed as the number of molecules per simulation cell is increased, as expected from the Central Limit Theorem.<sup>27</sup> This is consistent with simulation data reported for amorphous polymeric structures and is attributed to the inability of small simulation sizes to effectively sample the 3-D molecular arrangement and pore structures.<sup>28</sup> Upon increasing the sample size to 100 or more molecules per simulation cell, the simulations converge to a density and surface area in reasonable agreement with the experimentally reported surface area.<sup>14</sup> For systems of 50 molecules or less, the simulated surface area overlaps the experimental value, but the standard deviation is over 18%. This analysis highlights the importance of employing large molecular sample sizes to capture, with minimal variance, the density and porosity of amorphous materials.

To further highlight the importance of sample size in molecular amorphous materials, we measured the radial distribution functions (RDFs) of the molecular centers-of-mass for the systems with 25, 50, and 100 molecules per simulation cell, as shown in Figure 6. The RDF measures the density distribution of cage molecules around a cage molecule centered at the origin. It is clear from this plot that structural correlations between molecules extend beyond half the simulation box length for samples of less than 50 molecules. This means that a molecule could be spatially correlated with more than one periodic image of another particle, potentially introducing unphysical structural correlations that would make the simulated structure unrepresentative of that of an extended amorphous system. In contrast, the RDF of the sample containing 100 molecules converges to one at half the box length and thus finite-size effects should not be significant in this system.

**Amorphous Networks of **CC1**, **CC3**, **CC5**, **D1**, and **M1–M3**.** We applied the methodology outlined in Figure 2 to seven reported cage systems: **CC1**, **CC3**, **CC5**, **D1**, and **M1–M3**

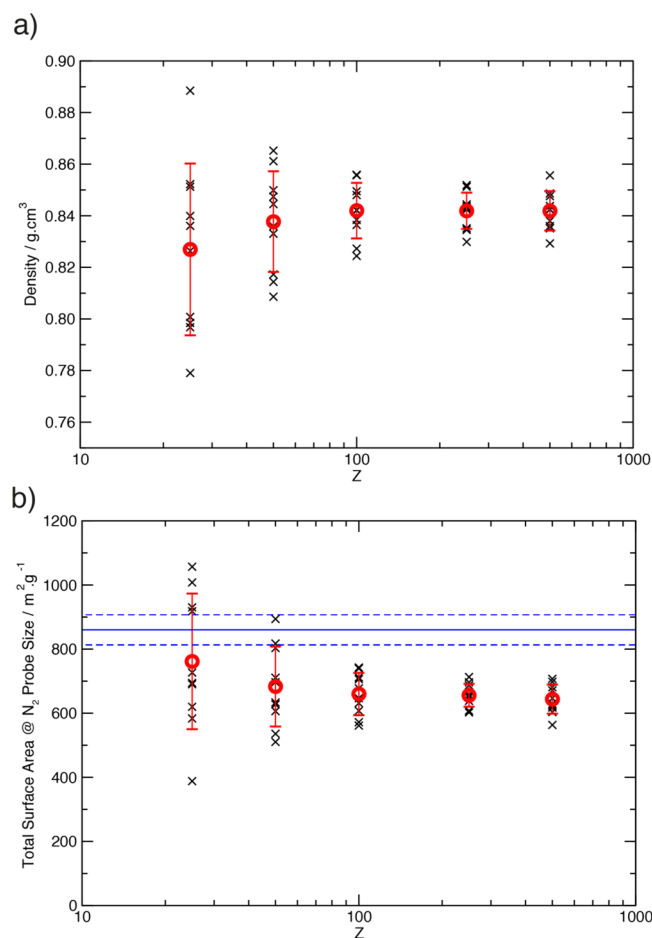


**Figure 5.** (a) Density and (b) total surface area of amorphous CC3 structures as a function of number of molecules per simulation cell ( $Z$ ). Data from unique simulations are depicted as crosses (black) and the average over these simulations is shown as circles (red). A blue solid line denotes the experimental surface area, with the error depicted as a blue dotted line.

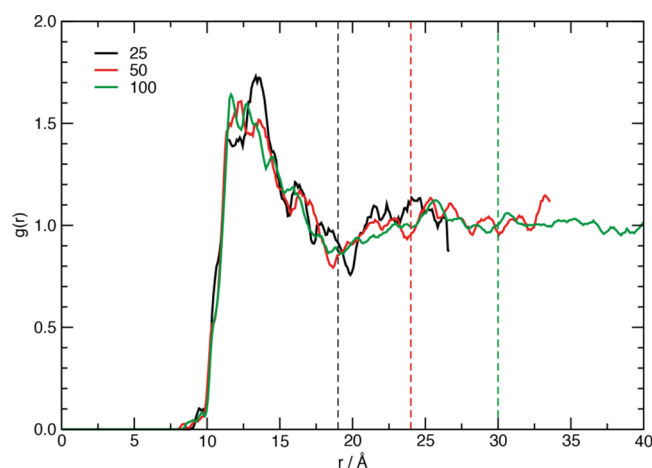


**Figure 6.** Radial distribution functions (RDFs) for the cage center-of-mass for samples of CC3 with 25, 50, and 100 molecules per simulation cell. Half-cell lengths are depicted by vertical dotted lines.

(Figure 1), resulting in structural models of amorphous networks with average densities listed in Table 1. We note that the density of the amorphous networks lies between  $0.566$  and  $0.873\text{ g}\cdot\text{cm}^{-3}$  and varies significantly for the selected cage

**Table 1. Resulting Amorphous Cell Densities**

cage	density/ $\text{g}\cdot\text{cm}^{-3}$
CC1	$0.873 \pm 0.013$
CC3	$0.842 \pm 0.011$
CC5	$0.658 \pm 0.018$
D1	$0.791 \pm 0.010$
M1	$0.838 \pm 0.018$
M2	$0.671 \pm 0.023$
M3	$0.556 \pm 0.017$

molecules. The densest amorphous structure is observed for CC1 as a consequence of the smaller cage volume and bare external functionality. By comparison, a much less dense structure is found for M3 as a result of the large cage volume and bulky external triphenylmethyl moieties.

To aid in the comparison of supramolecular arrangements, we calculated the radial distribution function for the centers-of-mass of each of the cages in the simulation cell. The average RDF from the 10 independent simulations for each of the seven cage systems is displayed in Figure 7. The RDFs calculated for networks of CC1, CC3, and CC5 (Figure 7a) demonstrate the effect of external functionality and cage size on the supramolecular arrangement of the molecular units. Attachment of sterically demanding cyclohexyl moieties in CC3 yields a broad distribution, an effect of the cyclohexyl groups directing the cage units to pack into a less dense network than the functionally bare units of CC1. The distribution is broadened further and displaced to greater distance as a consequence of the larger cage size of CC5 generating an increased average cage–cage distance of  $\sim 15\text{ \AA}$ , thus producing low-density amorphous structures. The first peak in the RDF of D1 (Figure 7b), unlike that in the RDFs of CC1, CC3, and CC5, does not correspond to the size of the molecule, with significant density observed at distances less than  $10\text{ \AA}$ . This behavior can be attributed to the elongated pyramidal geometry of the cage unit, which allows the units to pack in a dense interdigitated fashion, as shown in Figure 8. Finally, the calculated RDFs for the amorphous structures of M1–M3 provide further evidence that bulky functional groups yield inefficient packing and larger cage–cage distances. For example, increasing the external functional groups from methyl (M1) to *t*-butyl (M2) and triphenylmethyl (M3) results in a broadening of the primary RDF peak and a displacement to a larger average distance.

**Pore Structure Analysis of CC1, CC3, CC5, D1, and M1–M3: Role of Extrinsic Porosity.** The bulk porosity of the amorphous networks was probed by Voronoi network analysis. Pore volumes and surface areas were simulated using probe sizes equivalent to the kinetic diameters of He ( $2.60\text{ \AA}$ ) and  $\text{N}_2$  ( $3.64\text{ \AA}$ ), respectively, to give the resulting average values in Table 2. The average pore volume is plotted against the intrinsic cage volume and radius of gyration in Figure 9. The radius of gyration was used as a measure of the size of the cage molecule. Our simulations show no correlation between the cage volume and total pore volume. For example, a large difference in pore volume is observed for the series M1–M3 as a result of external functionality influencing the pore structure, but the cage volume itself does not vary across this series of molecules. In addition, in spite of the large cage volume of D1, the resulting pore volume is modest by virtue of the close packing of molecular units. In contrast to the lack of correlation for cage volume, there is a general trend for porosity with the radius of gyration, which varies with both the internal cage

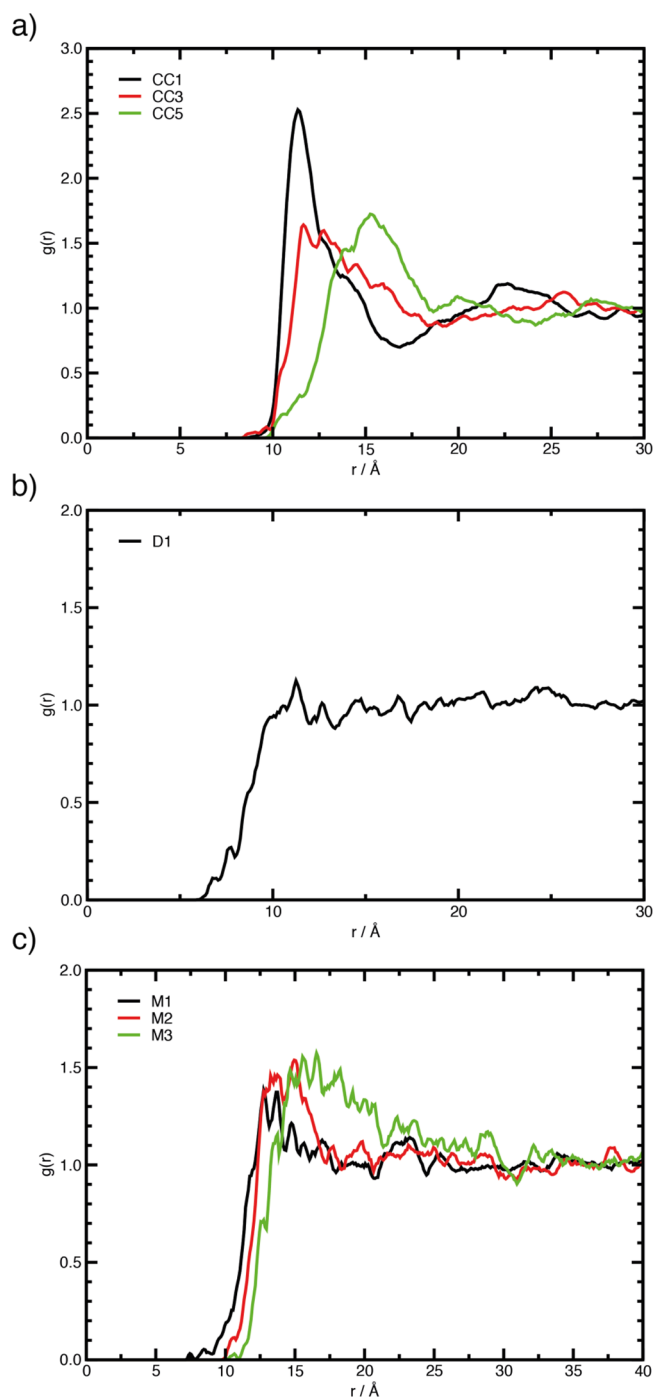


**Figure 7.** RDFs for the cage center-of-mass for structures (a) CC1, CC3, and CC5; (b) D1; and (c) M1–M3.

volume and external functionality (Figure 9b). For instance, the largest radii of gyration are a result of bulky external functionality (M3) or large cage structure (CC5), which in turn produce amorphous pore networks of large volumes and surface areas. From these results we can qualitatively conclude that molecules with large size produce amorphous structures with high surface areas and pore volumes and that this can be achieved by either constructing large cages or by decorating the surface of the cage with sterically bulky groups.

To further understand the porosity in these systems, pore size distributions were calculated and averaged over the 10 independent simulations; the distributions are depicted in

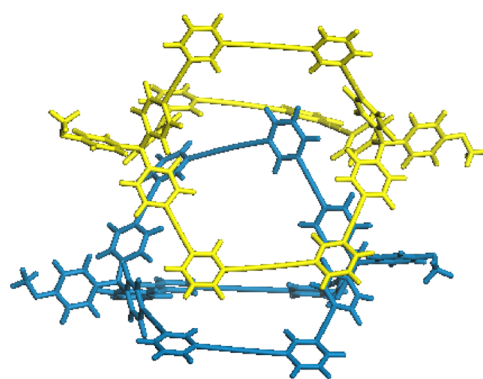


**Figure 8.** Representation of the interdigitated motif observed in amorphous structures of D1.

**Table 2. Average Total Surface Areas for N<sub>2</sub> Probe Size and Total Pore Volume for He Probe Size for the Amorphous Cage Structures**

cage	total surface area/m <sup>2</sup> ·g <sup>-1</sup>	total pore volume/cm <sup>3</sup> ·g <sup>-1</sup>
CC1	528 ± 77	0.076 ± 0.021
CC3	660 ± 66	0.097 ± 0.013
CC5	1815 ± 73	0.377 ± 0.034
D1	1211 ± 70	0.187 ± 0.012
M1	1168 ± 95	0.186 ± 0.021
M2	1759 ± 100	0.410 ± 0.044
M3	1892 ± 73	0.722 ± 0.056

Figure 10. Pore size distributions were simulated using the Zeo++ code; details of this method have been reported previously.<sup>29</sup> Cage CC1, as the result of close packing of cage units, has a pore size distribution with a sharp peak at ~5 Å. Sholl and co-workers have shown that materials with sharp and rigid pore size distributions are amenable to kinetic gas separations.<sup>30</sup> Importantly, this has been observed experimentally with amorphous samples of CC1 prepared by freeze-drying, which possess excellent H<sub>2</sub>/N<sub>2</sub> selectivity.<sup>14</sup> The pore structure of CC3 differs from that of CC1, with exohedral cyclohexane groups supporting larger pore diameters with sizes of 5–10 Å. Notably, CC1 and CC3 possess identical cages and this results in their pore networks having equivalent limiting pore sizes. Finally, the pore structure of CC5 has a broad distribution, owing to the combination of the large cage volume and bulky external functionality. The pore size distributions of M1–M3 clearly demonstrate the increase in porosity supported by increasingly bulky moieties. First, the distribution for M1 reflects the internal cage cavities, as the peak observed is equivalent to the internal diameter of the molecular cage. In comparison, M2 and M3 have larger molecular size increased by the attachment of bulky functionality. This produces broader pore size distributions as the disruption of close packing by the external functionality creates large extrinsic voids. Experimentally, Mastalerz and co-workers found that amorphous materials of M1–M3 had similar BET surface area.<sup>15</sup> However, these materials were analyzed as synthesized, not produced amorphously on purpose and thus may not be truly amorphous networks.

Amorphous molecular cage structures differ from their polymer analogues, as the source of disordered porous networks made from molecular cages differ fundamentally from their polymer analogues in that porosity can originate from two distinct sources: the internal cavity of the molecule

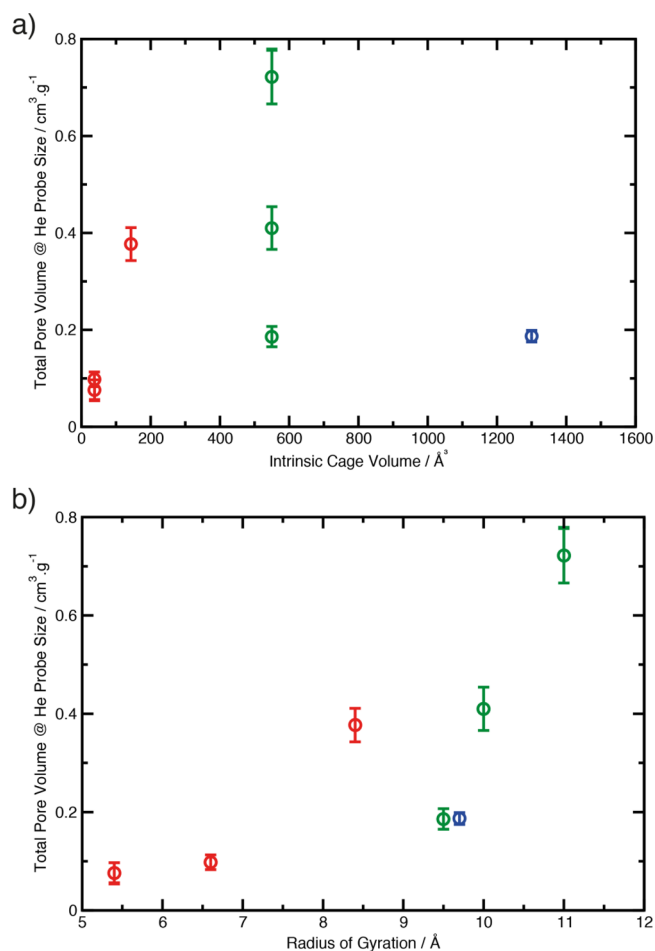


**Figure 9.** Average total pore volume for He probe radius against the (a) intrinsic cage volume and (b) radius of gyration. CC1, CC3, and CC5 (red), D1 (blue), and M1–M3 (green).

(intrinsic porosity) and the space external to the molecules formed by the supramolecular arrangement (extrinsic porosity). It is important to consider the source of the porosity when discussing the pore structure in these materials; as such the intrinsic and extrinsic pore volumes were measured in our generated systems, with the results displayed in Figure 11. Importantly, the amount of extrinsic porosity observed for CC1 and CC3 amorphous systems is equivalent to estimates previously reported; the larger cyclohexyl groups in CC3 produce a greater extrinsic volume by disrupting close packing. Increasing the cage size in CC5 results in an amorphous network with a slightly smaller ratio of extrinsic:intrinsic volume compared with CC3, as the intrinsic volume of the cage is larger but the external packing is similar to that of CC3. In contrast, D1 has significantly less extrinsic porosity than CC1, CC3, and CC5, as shown in Figure 11b, as a result of the molecular units packing in close proximity, which interconnects cage volumes. Finally, the trend in pore volume and pore size distributions for M1–M3 is clearly explained by the extrinsic pore percentage. Cages with bulky external moieties, such as M3, support large extrinsic voids, as depicted in Figure 11c. This packing results in broad and undefined pore sizes, as observed in the pore size distributions. In summary, the source of porosity in these materials is vital to understand the trends in porosity observed in this study: we find an increase in porosity

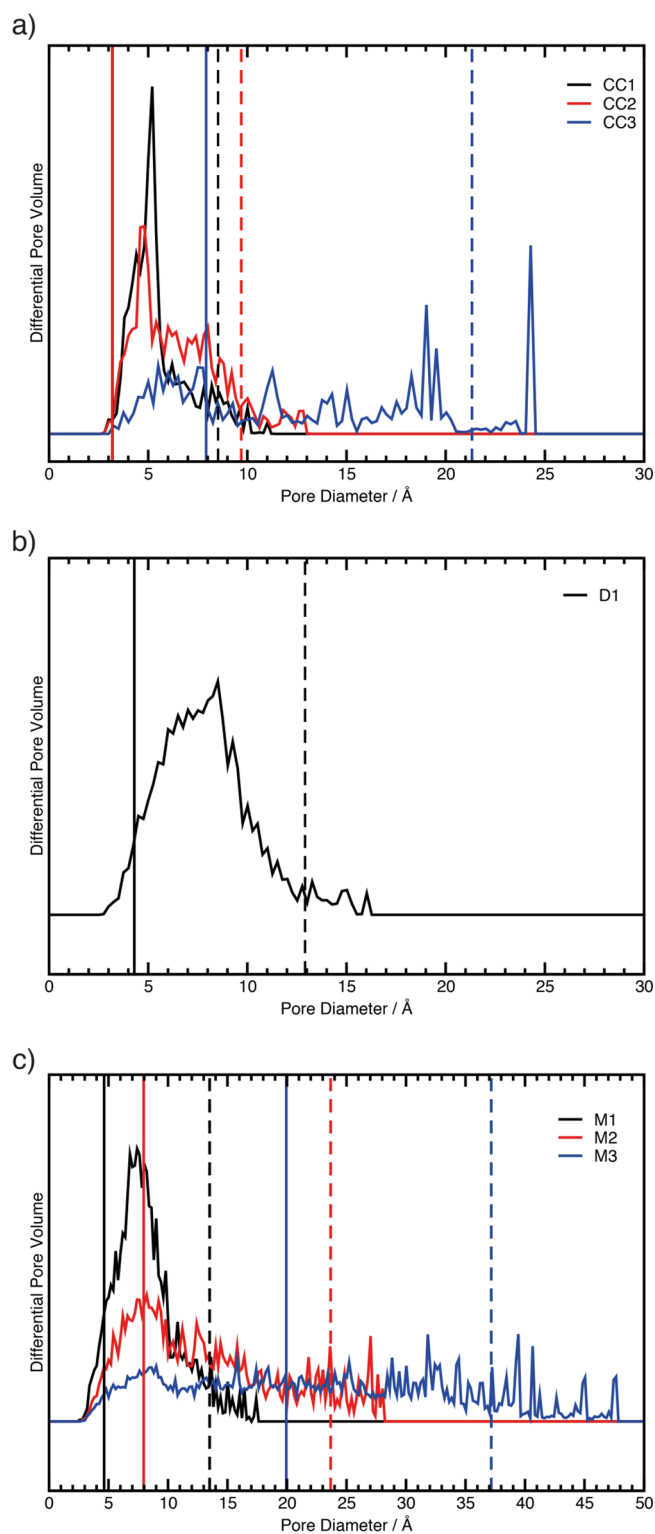


**Figure 10.** Pore size distributions for the amorphous networks resulting from structures (a) CC1, CC3, and CC5, (b) D1, and (c) M1–M3, along with average limiting pore diameter (vertical solid line) and average largest pore diameter (vertical dotted line).

in these amorphous systems is primarily a result of increasing the extrinsic porosity.

The potential advantages of amorphous networks are clearly evident when their surface areas and densities are compared with those of their crystalline counterparts. For example, SI

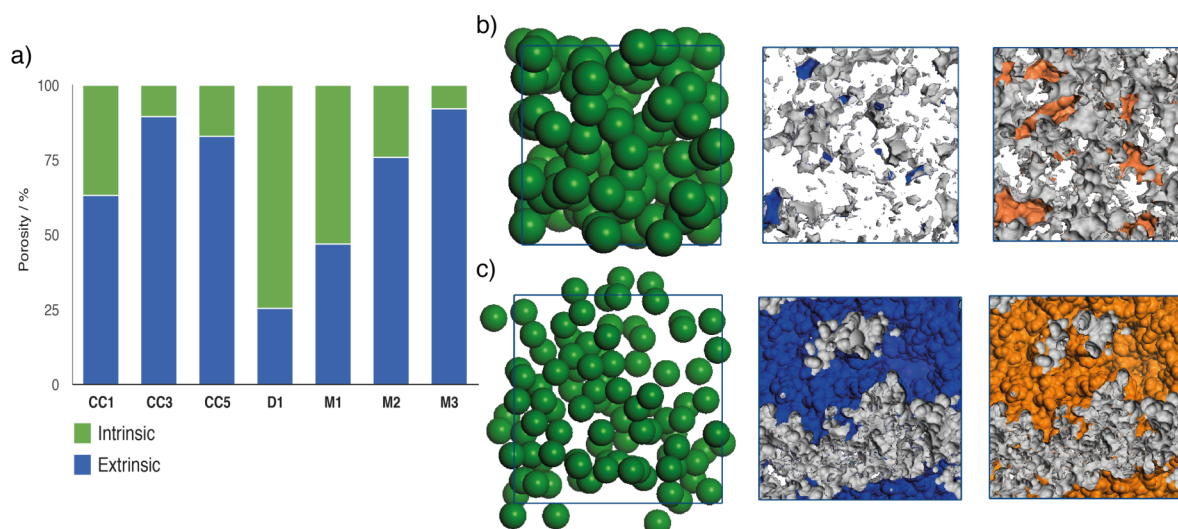


**Figure 11.** (a) Averaged contribution to the pore structure from intrinsic and extrinsic porosity and an example for (b) **D1** and (c) **M3**, with green spheres denoting the intrinsic pore structure, blue regions showing the extrinsic pore structure, and orange regions illustrating the total.

Table SI-4 shows how amorphous packing is able to unlock porosity that may not be possible to realize in crystalline polymorphs.

**In Silico Design of D1 Analogues.** The analysis above has outlined several general principles for designing the porosity of amorphous cage molecules. We sought to use these observations to optimize **D1** analogues for increased surface area in the amorphous state. The present study has found two general strategies, applied to the molecular units, to increase the porosity of amorphous cage systems: increasing the encapsulated cage volume (**CC3** and **CC5**) and introducing sterically bulky groups to the external surface of the cage (**M1–M3**). Accordingly, we have applied these principles to **D1** in the effort to produce an extremely porous structure. The hypothetical structure **D2** was realized by increasing the volume of **D1** by incorporation of phenyl rings to the dialkyne struts. Furthermore, a cage with bulky external functionality, **D3**, was constructed by adding mesityl groups to the vertices of **D1**. The two **D1** analogues, both shown in Figure 1, were selected to be synthetically feasible.

The density, surface area, and pore volume of amorphous cage networks for the **D1–D3** series is displayed in Table 3. It

**Table 3. Average Densities, Total Surface Areas, and Pore Volumes for Amorphous Structures D1–D3**

cage	density/ $\text{g}\cdot\text{cm}^{-3}$	total surface area/ $\text{m}^2\cdot\text{g}^{-1}$	total pore volume/ $\text{cm}^3\cdot\text{g}^{-1}$
<b>D1</b>	$0.791 \pm 0.010$	$1211 \pm 70$	$0.187 \pm 0.012$
<b>D2</b>	$0.859 \pm 0.011$	$804 \pm 66$	$0.118 \pm 0.011$
<b>D3</b>	$0.593 \pm 0.024$	$1933 \pm 70$	$0.554 \pm 0.069$

is clear that the larger volume cage **D2** structure produces an amorphous network with higher density and lower surface area and pore volume than the original **D1**. In contrast, functionalization by bulky mesityl groups in **D3** results in a less dense amorphous structure with increased surface area and pore volume.

Examination of RDFs in Figure 12a reveals the underlying reason for these observations. The increased cage size of **D2** not only produces large internal volume but also generates larger molecular windows and greater flexibility. A consequence

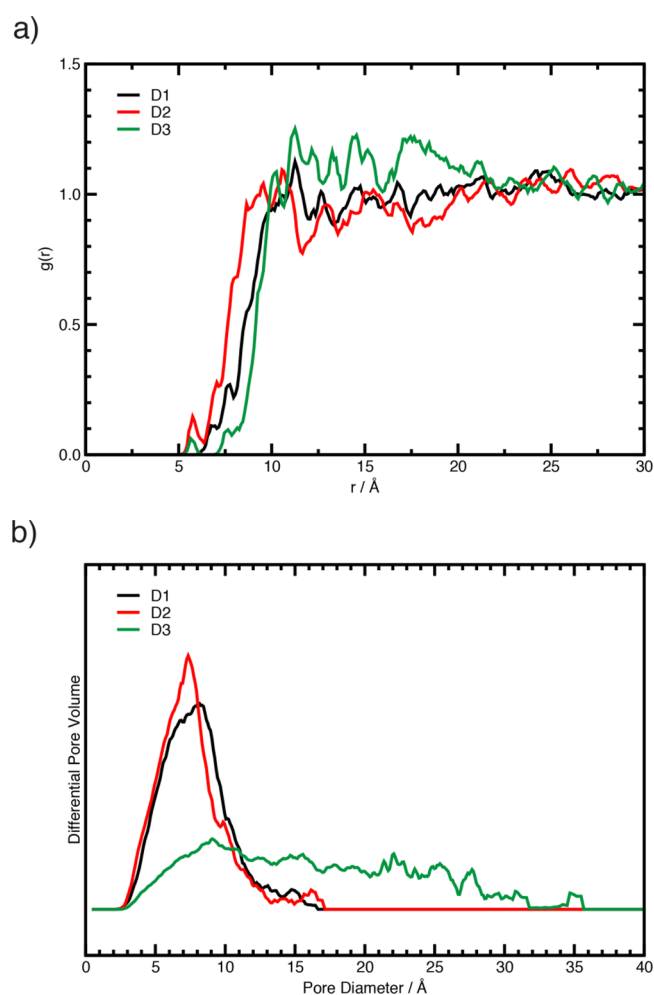


**Figure 12.** Average (a) RDFs and (b) pore size distributions for **D1–D3**.

of this is a greater degree of interdigitation, as evidenced by the peak in the RDF at shorter distances and higher density compared with **D1**. In contrast, the RDF for amorphous structures of **D3** is displaced to larger distance and broadened.

Absence of close packing cages at  $<8 \text{ \AA}$  and the broad distribution suggests that the mesityl functionality disrupts the close-packing motif observed for **D1** and **D2**. Additionally, calculation of the ratio of extrinsic:intrinsic porosity of the amorphous networks supports this conclusion, as shown in SI Table SI-5. Porosity for **D1** and **D2** structures is primarily a consequence of the intrinsic volume of the molecular cages, whereas **D3** has 76% of its pore volume associated with regions extrinsic to molecular units. Furthermore, the pore size distribution (Figure 11b) for **D3** demonstrates larger pore sizes are present in the amorphous system and the lack of defined pore sizes observed for **D1** and **D2**.

We have successfully tested the amorphous networks of hypothetical analogues of **D1** for porosity and morphology. In contrast to what was found for the **CC1** analogues, **CC3** and **CC5**, we find that increasing the internal volume in **D2** results in lower porosity due to the shape of molecular units allowing closer packing. However, by increasing the steric bulk external to the cage, as observed for **M1–M3**, we find the structure **D3** has increased pore volume and surface area, making this cage molecule an ideal candidate for synthesis.

## CONCLUSION

Herein we describe an efficient computational methodology for generating representative amorphous cells composed of porous organic cages. Importantly, we have improved significantly on previously reported methods through the use of external pressure during the compression stage and the use of GPU-accelerated molecular dynamics. Moreover, we have examined the porosity and morphology of the structures using Voronoi network analysis and center-of-mass radial distribution functions. We find good agreement between the simulated surface area of our **CC3** model and previously reported adsorption experiments. It is clear that the models described in this study give fundamental insight into these amorphous materials, which is unobtainable by experimental methods alone.

Our investigation has elucidated several important features of the nature of porous organic cage amorphous networks. First, on the subject of generation of representative amorphous models, we have demonstrated a modest effect of system size on the resulting density and porosity of the generated amorphous structure. Specifically, the **CC3** system demonstrates a large variance in the density and porosity of systems comprising less than 100 molecules per simulation cell. This result directed our methodology to use simulation cells of 100 molecules to ensure an accurate and precise representation of random packing of cage units. Second, we have gleaned general principles that govern the morphology and porosity in the amorphous state by applying our methodology to seven reported cage structures encompassing several distinct molecular geometries. Two key relationships are observed: a large encapsulated internal volume of the cage molecule can produce high-porosity amorphous structures (**CC5**), and bulky external functionality can yield highly porous structures by supporting greater pore volume extrinsic to the molecular units (**M3**). However, cage geometry is crucial to defining the resulting morphology. In particular, we find that the cage **D1** is able to interdigitate and consequently produces amorphous networks with unexceptional pore volume despite the large internal volume and cage size. Lastly, we have applied this understanding to optimizing the surface area of hypothetical analogues of **D1**. A novel analogue, **D3**, with bulky mesityl

groups attached external to the cage was found to produce an amorphous structure with increased porosity as a consequence of extrinsic pore volume.

This investigation has unequivocally demonstrated that molecular simulations can give atomistic insight into amorphous porous organic cages. This has allowed us to carry out de novo design of amorphous solids for applications in gas storage, which has previously only been applied for crystalline porous solids.

## ASSOCIATED CONTENT

### Supporting Information

Structural features, high-pressure crystalline simulations, blocking sphere diameters, crystalline porosity, and extrinsic:intrinsic pore volumes for **D1–D3**. This material is available free of charge via the Internet at <http://pubs.acs.org>.

## AUTHOR INFORMATION

### Corresponding Authors

\*aaron.thornton@csiro.au.

\*christian.doonan@adelaide.edu.au.

### Author Contributions

The manuscript was written through contributions of all authors. All authors have given approval to the final version of the manuscript.

### Notes

The authors declare no competing financial interest.

## ACKNOWLEDGMENTS

A.W.T. and J.D.E. acknowledge the Computational and Simulation Sciences Transformational Capability Platform at the CSIRO for funding and resources. D.S.S. acknowledges support from the U.S. Department of Energy Office of Basic Energy Sciences under award DE-FG02-12ER16362 as part of the Nanoporous Materials Genome Center. C.J.D. thanks the Australian Research Council for Funding (DP120103909 and FT100100400).

## REFERENCES

- (1) Lee, J.; Farha, O. K.; Roberts, J.; Scheidt, K. A.; Nguyen, S. T.; Hupp, J. T. Metal–organic Framework Materials as Catalysts. *Chem. Soc. Rev.* **2009**, *38*, 1450–1459.
- (2) Morris, R. E.; Wheatley, P. S. Gas Storage in Nanoporous Materials. *Angew. Chem., Int. Ed.* **2008**, *47*, 4966–4981.
- (3) Li, J.-R.; Sculley, J.; Zhou, H.-C. Metal–Organic Frameworks for Separations. *Chem. Rev.* **2012**, *112*, 869–932.
- (4) Cooper, A. I. Nanoporous Organics Enter the Cage Age. *Angew. Chem., Int. Ed.* **2011**, *50*, 996–998.
- (5) Furukawa, H.; Cordova, K. E.; O’Keeffe, M.; Yaghi, O. M. The Chemistry and Applications of Metal–Organic Frameworks. *Science* **2013**, *341*, 1230444.
- (6) Davis, M. E. Ordered Porous Materials for Emerging Applications. *Nature* **2002**, *417*, 813–821.
- (7) Evans, J. D.; Huang, D. M.; Hill, M. R.; Sumbly, C. J.; Thornton, A. W.; Doonan, C. J. Feasibility of Mixed Matrix Membrane Gas Separations Employing Porous Organic Cages. *J. Phys. Chem. C* **2014**, *118*, 1523–1529.
- (8) Bushell, A. F.; Budd, P. M.; Attfield, M. P.; Jones, J. T. A.; Hasell, T.; Cooper, A. I.; Bernardo, P.; Bazzarelli, F.; Clarizia, G.; Jansen, J. C. Nanoporous Organic Polymer/Cage Composite Membranes. *Angew. Chem., Int. Ed.* **2013**, *52*, 1253–1256.
- (9) Tozawa, T.; Jones, J. T. A.; Swamy, S. I.; Jiang, S.; Adams, D. J.; Shakespeare, S.; Clowes, R.; Bradshaw, D.; Hasell, T.; Chong, S. Y.; et al. Porous Organic Cages. *Nat. Mater.* **2009**, *8*, 973–978.

- (10) Avellaneda, A.; Valente, P.; Burgun, A.; Evans, J. D.; Markwell-Heys, A. W.; Rankine, D.; Nielsen, D. J.; Hill, M. R.; Sumbly, C. J.; Doonan, C. J. Kinetically Controlled Porosity in a Robust Organic Cage Material. *Angew. Chem.* **2013**, *125*, 3834–3837.
- (11) Jones, J. T. A.; Holden, D.; Mitra, T.; Hasell, T.; Adams, D. J.; Jelfs, K. E.; Trewin, A.; Willock, D. J.; Day, G. M.; Bacsá, J.; et al. On–Off Porosity Switching in a Molecular Organic Solid. *Angew. Chem.* **2011**, *123*, 775–779.
- (12) Abbott, L. J.; Colina, C. M. Formation of Microporosity in Hyper-Cross-Linked Polymers. *Macromolecules* **2014**, *47*, 5409–5415.
- (13) Abbott, L. J.; McDermott, A. G.; Del Regno, A.; Taylor, R. G. D.; Bezzu, C. G.; Msayib, K. J.; McKeown, N. B.; Siperstein, F. R.; Runt, J.; Colina, C. M. Characterizing the Structure of Organic Molecules of Intrinsic Microporosity by Molecular Simulations and X-Ray Scattering. *J. Phys. Chem. B* **2013**, *117*, 355–364.
- (14) Jiang, S.; Jelfs, K. E.; Holden, D.; Hasell, T.; Chong, S. Y.; Haranczyk, M.; Trewin, A.; Cooper, A. I. Molecular Dynamics Simulations of Gas Selectivity in Amorphous Porous Molecular Solids. *J. Am. Chem. Soc.* **2013**, *135*, 17818–17830.
- (15) Schneider, M. W.; Oppel, I. M.; Ott, H.; Lechner, L. G.; Hauswald, H.-J. S.; Stoll, R.; Mastalerz, M. Periphery-Substituted [4 + 6] Salicylbisimine Cage Compounds with Exceptionally High Surface Areas: Influence of the Molecular Structure on Nitrogen Sorption Properties. *Chem. – Eur. J.* **2012**, *18*, 836–847.
- (16) Brown, W. M.; Wang, P.; Plimpton, S. J.; Tharrington, A. N. Implementing Molecular Dynamics on Hybrid High Performance Computers – Short Range Forces. *Comput. Phys. Commun.* **2011**, *182*, 898–911.
- (17) Plimpton, S. Fast Parallel Algorithms for Short-Range Molecular Dynamics. *J. Comput. Phys.* **1995**, *117*, 1–19.
- (18) Holden, D.; Jelfs, K. E.; Cooper, A. I.; Trewin, A.; Willock, D. J. Bespoke Force Field for Simulating the Molecular Dynamics of Porous Organic Cages. *J. Phys. Chem. C* **2012**, *116*, 16639–16651.
- (19) Sun, H. Ab Initio Calculations and Force Field Development for Computer Simulation of Polysilanes. *Macromolecules* **1995**, *28*, 701–712.
- (20) Pollock, E. L.; Glosli, J. Comments on P3M, FMM, and the Ewald Method for Large Periodic Coulombic Systems. *Comput. Phys. Commun.* **1996**, *95*, 93–110.
- (21) Evans, D. J.; Holian, B. L. The Nose–Hoover Thermostat. *J. Chem. Phys.* **1985**, *83*, 4069–4074.
- (22) Jelfs, K. E.; Schiffmann, F.; Jones, J. T. A.; Slater, B.; Cora, F.; Cooper, A. I. Conformer Interconversion in a Switchable Porous Organic Cage. *Phys. Chem. Chem. Phys.* **2011**, *13*, 20081–20085.
- (23) Jiang, S.; Jones, J. T. A.; Hasell, T.; Blythe, C. E.; Adams, D. J.; Trewin, A.; Cooper, A. I. Porous Organic Molecular Solids by Dynamic Covalent Scrambling. *Nat. Commun.* **2011**, *2*, 207.
- (24) Martin, R. L.; Smit, B.; Haranczyk, M. Addressing Challenges of Identifying Geometrically Diverse Sets of Crystalline Porous Materials. *J. Chem. Inf. Model.* **2012**, *52*, 308–318.
- (25) Willems, T. F.; Rycroft, C. H.; Kazi, M.; Meza, J. C.; Haranczyk, M. Algorithms and Tools for High-Throughput Geometry-Based Analysis of Crystalline Porous Materials. *Microporous Mesoporous Mater.* **2012**, *149*, 134–141.
- (26) Holden, D.; Jelfs, K. E.; Trewin, A.; Willock, D. J.; Haranczyk, M.; Cooper, A. I. Gas Diffusion in a Porous Organic Cage: Analysis of Dynamic Pore Connectivity Using Molecular Dynamics Simulations. *J. Phys. Chem. C* **2014**, *118*, 12734–12743.
- (27) Reichl, L. E. *A Modern Course in Statistical Physics*, 3rd revised and updated ed.; Wiley-VCH: Weinheim, 2009.
- (28) Hart, K. E.; Abbott, L. J.; Colina, C. M. Analysis of Force Fields and BET Theory for Polymers of Intrinsic Microporosity. *Mol. Simul.* **2013**, *39*, 397–404.
- (29) Pinheiro, M.; Martin, R. L.; Rycroft, C. H.; Jones, A.; Iglesia, E.; Haranczyk, M. Characterization and Comparison of Pore Landscapes in Crystalline Porous Materials. *J. Mol. Graph. Model.* **2013**, *44*, 208–219.
- (30) Haldoupis, E.; Watanabe, T.; Nair, S.; Sholl, D. S. Quantifying Large Effects of Framework Flexibility on Diffusion in MOFs: CH<sub>4</sub> and CO<sub>2</sub> in ZIF-8. *ChemPhysChem* **2012**, *13*, 3449–3452.